energy&fuels

pubs.acs.org/EF

Article

Modeling the Effects of Sedimentation on Natural Occurrences of CH_4 Hydrates in Marine Sediments

Alejandro Bello-Palacios,* Per Fotland, and Geir Ersland

Cite This: *Energy Fuels* 2022, 36, 3778−3787

Read Online

ACCESS | Metrics & More | Article Recommendations

ABSTRACT: This study explores the relationships that sedimentation rate and transport properties have with the formation and evolution of hydrates in fine-grained marine sediments and their corresponding bottom simulating reflector (BSR) responses. Using a series of one-dimensional simulations of multiphase, multicomponent flow and transport of mass and heat through porous media, a slab of sediments through sedimentation is modeled. The boundary conditions are set to emulate the pressure and geothermal gradients and its resulting gas hydrate stability zone (GHSZ). Hydrates are formed by injecting methane gas through the bottom of the grid and letting it migrate and reach the boundary of stability. The resulting hydrate accumulation is subjected to different sedimentation rates and replicated with different intrinsic permeability. With sedimentation, the geothermal gradient is displaced upward and the boundary of stability shoals. Through methane recycling, the distribution of phases changes through cycles of slow melting and rapid reformation. This results in a dynamic flow barrier that relocates the base of the GHSZ over geological time, in response to the variations of both pressure and salinity. The characteristics of a BSR response will be tied to the stage of the melting cycle.

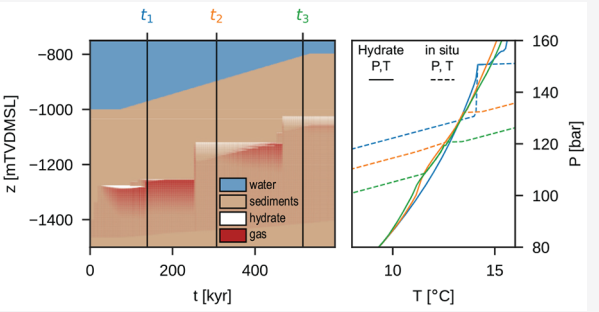

INTRODUCTION

Gas hydrates are crystalline ice-like solids formed by the mixing of water and gas under pressure. Water molecules form hydrogen-bonded structures with cavities that are stabilized by the filling of nonpolar or slightly polar guest gas molecules.[1]

In nature, methane is a predominant guest molecule[2] that forms hydrates at relatively low temperatures and high pressures.[1] Permafrost regions and deep marine sediments in the outer continental margins are known to host widespread accumulations of methane hydrates.[3] Estimates suggest that the latter hosts the majority of methane hydrates in nature.[4]

Several occurrences of deep marine hydrates have been identified and targeted for both scientific and commercial purposes. The International Ocean Discovery Program (IODP)/Ocean Drilling Program (ODP) scientific results from leg 164 at Blake Ridge,[5] leg 204 in the Hydrate Ridge in offshore Oregon,[6] and expedition 311 at the Northern Cascadia margin[7] have provided crucial data to study and monitor hydrate systems in this setting. The Nyegga pockmark field in offshore mid-Norway is another occurrence that has been studied in detail.[8] In addition, the governments of the U.S.A., Japan, South Korea, India, and China have initiated national-led programs to evaluate the economical prospectivity of hydrate occurrences in the Gulf of Mexico, Nankai Trough, Ulleung Basin, Krishna Godavari Basin, and South China Sea, respectively.[9]

The characteristics of these occurrences vary greatly in terms of their physical form and geological environment.[10] Some of the hydrate accumulations identified in both Blake Ridge[11] and the South China Sea[12] occur in fine-grained sediments with hydrates concentrated toward the base of the gas hydrate stability zone (GHSZ). Recycling of methane can explain the formation of such localized concentrations.[13,14] This mechanism works by active sedimentation driving hydrates out of the GHSZ. As the hydrates start melting, the expelled gas accumulates, driven by buoyancy, flows back into the GHSZ, and forms new hydrates. Methane migrating from far beneath the stability boundary can also enrich these hydrate accumulations.[15] The contrast in acoustic impedance caused by the interface between the expelled gas and hydrate can produce a bottom simulating reflector (BSR),[16] a seismic reflection that follows the shape of the seafloor and can coincide with the base of stability of hydrates.[17]

Numerical modeling has been crucial to study gas hydrate occurrences in geological systems.[10] It involves the use of fully

Received: October 22, 2021
Revised: February 26, 2022
Published: March 15, 2022

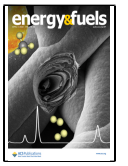

https://doi.org/10.1021/acs.energyfuels.1c03611
Energy Fuels 2022, 36, 3778−3787

coupled, multiphase, and multicomponent methane hydrate formation models. Multiple tools have been tested and compared[18,19] to validate and build confidence in the modeling of hydrate-related processes in porous media.

Some of these tools have been used to model deep marine hydrate systems. Using Blake Ridge as a case study, Burwicz and Rüpke[20] and You and Flemings[21] have thoroughly modeled the formation and evolution of a hydrate system with sediment burial and compaction. Focusing more on the mechanisms driving the concentration of hydrates, Nole et al.[22] developed a model to simulate methane recycling in marine hydrate systems. Similarly, Liu and Flemings[15] simulated hydrate formation from a methane source far beneath the GHSZ.

The TOUGH+HYDRATE (T+H) version 1.5[23,24] code and its open-source version HydrateResSim[25] are also publicly available codes that have taken part in code-comparison studies.[18,19] They have been used primarily to evaluate the methane production from natural hydrate systems.[26−29] In addition, T+H has been used to model systems over larger time scales representing geological processes.[30,31]

These numerical tools offer an opportunity to analyze the complexities of these natural systems. These tools are capable of simulating multiple processes occurring simultaneously at different spatial and time scales. To do this, they have to account for the dynamic effects of hydrate formation and dissociation on salinity, temperature, pressure, and transport properties.[15]

This study looks at how the physical form of a hydrate occurrence can be affected by changes in both geology and environment. Special focus is given to the role of sedimentation on the evolution of an already established methane hydrate occurrence. In each simulation, all variations in the temperature, pressure, phase saturation, and concentration of soluble components among other parameters are logged. This information is used to describe the occurring mechanisms that mark the evolution of a hydrate occurrence and to explain how the geological history of a basin can determine the expression of a BSR.

METHODS

All simulations were performed in T+H. Developed by Lawrence Berkeley National Laboratory (LBNL), it simulates the behavior of methane-hydrate-bearing sediments and handles both multiphase, multicomponent flow and transport of mass and heat through porous and fractured media.[23,24] An overview of the simulation runs included in the results is shown in Table 1.

In T+H, hydrate formation and dissociation are modeled using either an equilibrium or kinetic model. Kowalsky and Moridis[32] have compared both approaches and concluded that they are practically indistinguishable. Kinetic limitation becomes important in short-term processes or core-scale simulations. Thus, this study uses the equilibrium approach only.

In the equilibrium model, phase transitions are governed only by pressure and temperature. Water and methane are mass components, and hydrate is one of the potential phases that can be present in different combinations (Figure 1).

Modeling Approach and Initialization. The simulation grid consists of a one-dimensional (1D) representation of marine sediments. The total thickness modeled is 600 m with a vertical resolution of 1 m. Thermophysical properties and parameters used in the simulations are included in Table 2.

The grid is initialized fully saturated by brine (3.5 wt % NaCl), and boundary conditions at the top and bottom of the grid are set to emulate the natural pressure and temperature gradients of seafloor

Table 1. Overview of Simulation Runs

case number	modeled process	based on
1A	hydrate formation without scaling k and P_{ce} k = 10 mD	
1B	hydrate formation with scaling k and P_{ce} k = 10 mD	
1C	hydrate formation with scaling k and P_{ce} k = 10 μD	
2	hydrate evolution in an idle system no sedimentation rate; no gas source	1B
3A	hydrate evolution with sedimentation sedimentation rate = 220 mm/year; no gas source	1B
3B	hydrate evolution with sedimentation; k = 10 μD sedimentation rate = 220 mm/year; no gas source	1C
4	hydrate evolution with sedimentation sedimentation rate = 2 m/year; no gas source	1B

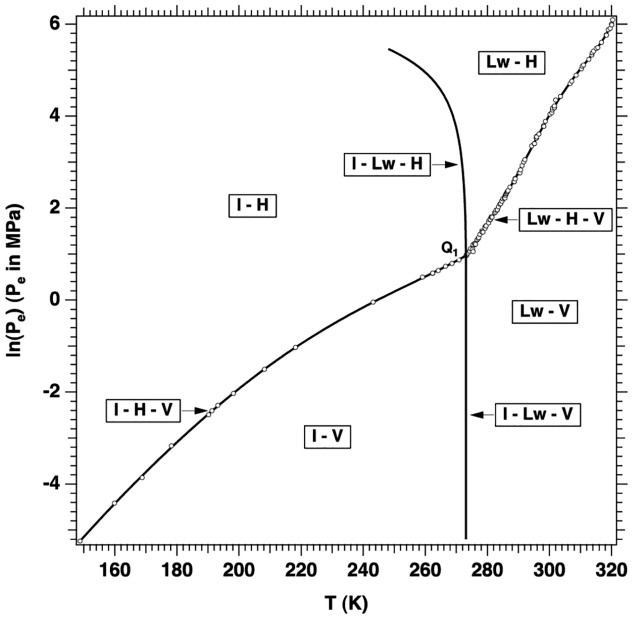

Figure 1. Pressure−temperature equilibrium relationship in the phase diagram of the water−methane−hydrate system. All possible combinations of the four phases are displayed: aqueous (Lw), ice (I), gas (V), and hydrate (H).[24]

sediments at 1000 m below mean sea level (Figure 2). At the top of the grid, a series of layers represent the water column and are set as an infinite boundary that keeps the pressure and temperature constant. At the bottom of the grid, a constant heat source emits the necessary heat to reach a thermal gradient close to 50 °C/km. Compaction of sediments is not considered; therefore, the initial intrinsic transport properties do not change along the thickness of the simulation grid.

We set an adjacent grid placed on each side of the main grid. The horizontal permeability between the main grid and these adjacent grids is zero through the largest part of the thickness (left panel of Figure 2). Fluid flow between these is possible only near the top or bottom of the grid. The purpose of this setup is to keep the pressure at the top and bottom of the grid always connected. In this manner, the restriction of flow caused by hydrates does cause pressure compartmentalization of the grid.

Hydrate Formation. Once the model is initialized and with a representative gradient of pressure and temperature, a flux of methane is initiated. The objective is to generate a hydrate accumulation as the buoyancy-driven flux of methane reaches the base of the GHSZ. The gas source delivers 12 kg of methane per millennium (kg of CH_4 m^{-2}

https://doi.org/10.1021/acs.energyfuels.1c03611
Energy Fuels 2022, 36, 3778−3787

Table 2. Thermophysical Properties of Materials and Parameters Used in the Simulation Model

parameter	value
gas composition	100% CH_4
intrinsic permeability, $k_x = k_y = k_z$	1 mD (9.86×10^{-16} m^2)
intrinsic porosity, ϕ_0	0.30 fraction
density, ρ	2650 kg/m^3
brine salinity, X_{inh}	3.5 wt %
thermal conductivity, dry, λ_d	0.30 W m^{-1} K^{-1}
thermal conductivity, fully saturated, λ_w	1.40 W m^{-1} K^{-1}
specific heat, c_p	1400 J kg^{-1} K^{-1}
composite thermal conductivity model, λ	$\lambda = \lambda_d + (S_W^{1/2} + S_H^{1/2})(\lambda_w - \lambda_d)$
modified relative permeability model[33]	$k_{rA} = ((S_W - S_{irW})/(1 - S_{irW}))^{n_W}$ $k_{rG} = ((S_G - S_{irG})/(1 - S_{irG}))^{n_G}$ $k_{rH} = 0$ $n_W = 4.0$; $n_G = 2.0$ $S_{irW} = 0.11$; $S_{irG} = 0.02$
capillary pressure model[34]	$P_{cap} = -P_0\,[(S^*)^{-1/\gamma} - 1]^{1-\gamma}$ $S^* = ((S_W - S_{irW})/(S_{mxA} - S_{irW}))$ $\gamma = 0.7$; $S_{irW} = 0.1$ $P_0 = 22.2$ bar; $S_{mxA} = 1.0$
diffusion coefficients	1×10^{-10} m^2/s NaCl(aq) 1×10^{-10} m^2/s CH_4(aq) 1×10^{-5} m^2/s H_2O(g)
pressure at the top boundary (seabed)	104.5 bar at 1000 mTVDMSL
temperature at the top boundary (seabed)	0.1 °C (273.25 K)
basal heat flow rate	75 mW/m^2
methane source gas flow rate	12 kg of CH_4 m^{-2} kyr^{-1}
geothermal gradient	50 °C/km

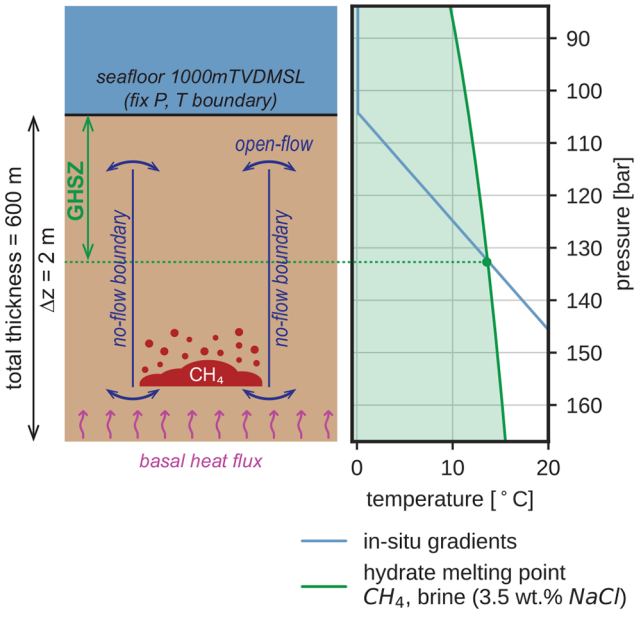

Figure 2. Schematic representation of the simulation model. The figure on the left shows the principal elements represented by the simulation model. The chart on the right shows the pressure and temperature at which the system is initialized (blue), superimposed by the curve representing the boundary of stability for CH_4 hydrate and 3.5 wt % brine NaCl. The green-shaded region highlights the P and T ranges, where hydrates are stable. The crossing between these two is defined as the base of the GHSZ.

kyr^{-1}). After 75 kyr, the simulations are arbitrarily stopped. At this point, the resulting distribution of phases and salinity might not equilibrate. Pressure buildups and peaks in the concentration of salinity will accompany the formation of hydrates. However, if the system is left to respond only to the boundary conditions and without a gas source, the time needed to bring it back to equilibrium will be longer than any of the processes modeled in this study.

T+H can modify transport properties (i.e., porosity, permeability, and capillary entry pressure) as a function of hydrate saturation (S_H). We model hydrate formation both with (case 1A) and without (case 1B) modification of transport properties. This alteration is expected to limit the fluid flow, increasing the concentration of hydrate toward the bottom of the GHSZ.

The modification of transport properties is defined by an evolutionary porosity model.[23] In this model, the hydrate is considered an extension of the matrix. The resulting effective porosity (ϕ) is equivalent to the intrinsic porosity (ϕ_0) reduced by the solid hydrate phase, expressed in eq 1.

$$\phi = \phi_0(1 - S_H) \tag{1}$$

This change in porosity is reflected in a scaling of both permeability (k) and capillary entry pressure (P_c).

Scaling of permeability is defined by a permeability reduction factor k_{rF}, expressed in eq 2 (top panel of Figure 3).

$$\left(\frac{k}{k_0}\right) = k_{rF} = \left(\frac{\phi - \phi_c}{\phi_0 - \phi_c}\right)^m \tag{2}$$

The critical porosity ϕ_c accounts for scenarios of hydrates clogging pore throats and disconnecting fluid-filled pores. It is linked to the saturation of hydrates at which the effective permeability is reduced to zero.

As the porosity and permeability change, the Leverett model (eq 3) is used to scale the capillary pressure (bottom panel of Figure 3). The input capillary pressure function was defined to match capillary pressure measurements from fine-grained marine sediments from the Gulf of Mexico[35] and Blake Ridge[36] regions. Both the hydrate-bearing and hydrate-free porosity and permeability from eqs 1 and 2 are used as inputs. Because hydrates are an extension of the matrix, the resulting scaled capillary pressure will reflect on the reduction of the effective radius of the pore throat.

$$P_c^* = P_c\sqrt{\frac{k_0}{k}\frac{\phi}{\phi_0}} \tag{3}$$

Sediment mechanics are not considered in these study. The formation of hydrates occurs uniformly and is constrained only by the pressure, temperature, salinity, and availability of methane and water.

Sedimentation Rate. Sedimentation is modeled by a series of continuous simulations. To emulate the process of sedimentation, the grid elements immediately above those representing the seafloor are progressively switched from an infinite boundary to a cell representing a new layer of sediment. The duration of each simulation is equivalent to the time it takes to deposit a 2 m thick layer at a given sedimentation rate. Assuming the temperature at the seafloor remains constant, the resulting temperature gradient is displaced upward. In response, the boundary of stability is progressively displaced in the same direction, forming a shallower and thinner GHSZ (Figure 4).

This setup is used to test how the previously formed hydrate occurrence responds to boundary conditions that change over time. Different sedimentation rates are tested, ranging from a low sedimentation rate (case 3, at 220 mm/year), comparable to that observed in the Blake Ridge,[37] to a system with higher sedimentation rates (case 4, at 2 m/year), comparable to those observed in places like the Nyegga area.[8] Particular attention is given to the process of methane recycling and how it affects the physical form of the final hydrate occurrence. For comparison, a simulation of an idle system where the boundary conditions remain unchanged is included in case 2.

https://doi.org/10.1021/acs.energyfuels.1c03611
Energy Fuels 2022, 36, 3778−3787

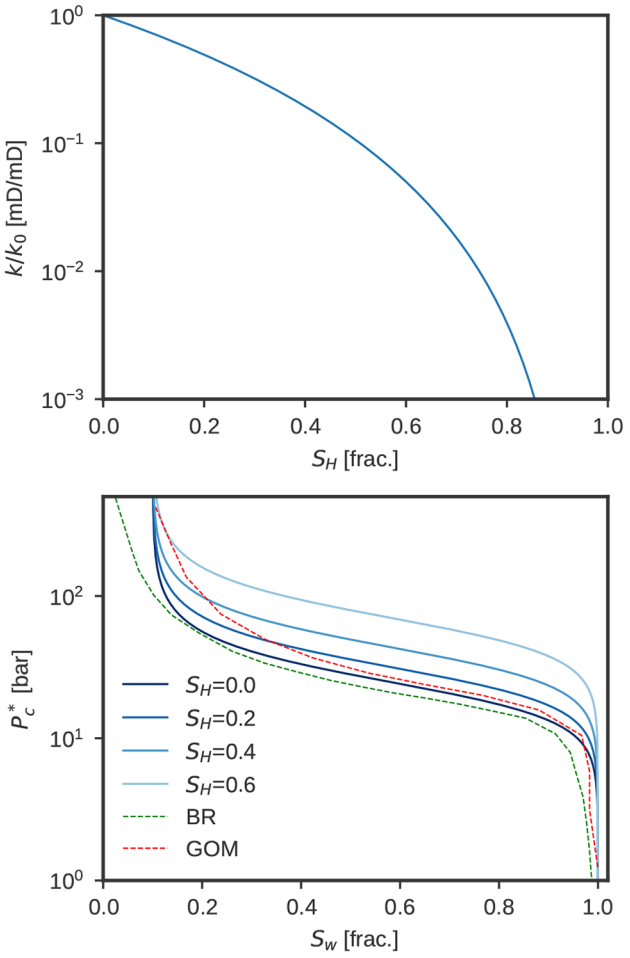

Figure 3. Scaling of both intrinsic permeability (top) and capillary pressure (bottom) in the presence of hydrates in T+H, with input parameters in Table 2. The initial capillary pressure curve (S_H = 0) was built using reference data from the Gulf of Mexico (GOM) and Blake Ridge (BR) sediments.[35,36]

Sediment compaction through burial is not considered in this study. As new layers are deposited, the transport properties remain unchanged.

RESULTS AND DISCUSSION

Initial Hydrate Formation. Two different hydrate accumulations were achieved during cases 1A and 1B. In both cases, the use of a capillary pressure curve (Figure 5) has modified the *in situ* pressure gradient with depth. With both gas and brine co-existing in the pores, the pressure in the gas phase has to overcome the capillary entry pressure of the given curve (near 10 bar). The resulting pressure gradients are no longer linear, and the excess pressure displaces the base of the GHSZ a few meters down (column 4 in Figure 5). In addition, the local increase of salinity that results from hydrate formation has also lifted the boundary of stability of hydrates.

In the cases where hydrate saturation did not affect the transport properties (top row of Figure 5), most methane was turned into hydrates. The resulting accumulation was a thick layer of hydrates (near 40 m) with residual gas only. Salinity increased locally to 6.4 wt % NaCl at the point of maximum hydrate saturation (68.7%).

Results varied greatly when hydrate saturation was used to scale both capillary pressure and permeability. As hydrates started forming, a smaller amount of gas was able to pass through the hydrate-saturated interval. The resulting accumulation concentrated in a thinner layer of hydrate. Because less hydrates have formed, the maximum salinity was 4.4 wt % NaCl. The remaining methane formed a gas accumulation trapped by hydrates. The capillary pressure resulting from this free gas accumulation displaced the base of the GHSZ further down.

The first scenario might produce a weak response not detectable as BSR. The second scenario would yield a stronger reflection. On the basis of these results, if the intrinsic capillary entry pressure of the host sediments is high, there would be a larger discrepancy in depth between the BSR and the thermodynamic phase boundary.

Evolution during Sedimentation. A useful feature of a numerical simulation like T+H is its capacity to keep track of all variables involved in hydrate transition phases and the transport of heat and mass. In complex systems, like those observed in this study, it becomes a powerful tool to understand the mechanisms behind the thermodynamic evolution of a hydrate occurrence over geological time. However, there are still limitations inherent to the simulator that constrain the capacity of this methodology. These limitations refer to the consideration of the mechanical properties of fine-grained sediments in two main processes: burial and compaction of sediments and the effects of hydrate formation in unconsolidated fine-grained sediments. For the first part, although it was possible to emulate the process of sedimentation by stacking up layers and updating the boundary condition, the resulting mechanical compaction of sediments was not represented. However, the base of the GHSZ, the interval where most melting and reformation occurs, represents a narrow interval in depth where the transport properties remain roughly constant over time. With regard to the second process, in fine-grained sediments, hydrates can form nodules and lenses that mechanically displace grains.[38] These processes can also have an impact on the effective transport properties of the system. Addressing these processes go beyond the scope of the simulator. Despite these considerations, the methods and results of this study are still meaningful and offer a building block in understanding the effects of hydrate formation on the transport properties of porous systems during sedimentation.

The simulations of the sedimentation rate showed the evolution of a hydrate accumulation over geological time. As expected, the temperature increase as a result of sedimentation caused hydrate melting. However, the rate of dissociation was asynchronous with the rate of sedimentation. The evolution of the hydrate−gas boundary follows a staircase pattern that does not follow the theoretical GHSZ that the *in situ* conditions of the pressure, temperature, and salinity would yield (Figure 6). Each step of this pattern represents a cycle where methane and hydrate reaccommodate following the local conditions.

Each cycle consisted of a period of fast growth of hydrates followed by slow melting. The length of the cycles was constrained by the rate at which the temperature increased (sedimentation) and the amount of hydrate that had formed at the beginning of each cycle. For the 220 mm/year sedimentation rate, at least two full cycles were observed (Figure 6). Melting started at the warmest and deepest intervals of the hydrate layer. Expelled methane reentered the gas column underneath, and the remaining hydrate became

https://doi.org/10.1021/acs.energyfuels.1c03611
Energy Fuels 2022, 36, 3778−3787

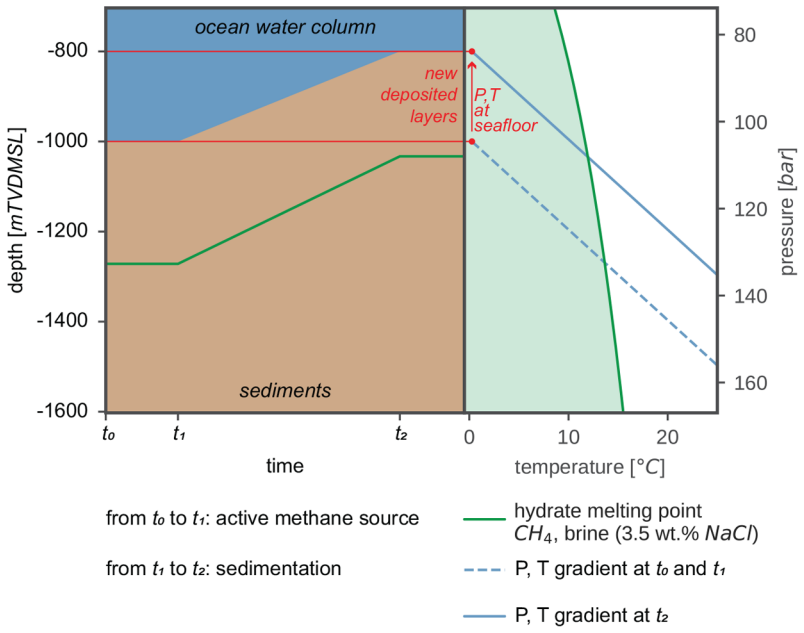

Figure 4. Schematic representation of how the sedimentation rate is modeled. On the left is a depth versus time chart showing how the sediment column changes over time. The methane gas source starts at t_0 and stops at t_1. At t_1, sedimentation starts and stops once it has deposited a thickness of 200 m. On the right is a P versus T chart displaying the boundary of stability (green) and the *in situ* P and T gradients at t_0, t_1, and t_2. The green-shaded region highlights the P and T ranges, where hydrates are stable. The depth at which the *in situ* gradients cross the stability boundary over time is displayed on the right and defines the base of the GHSZ.

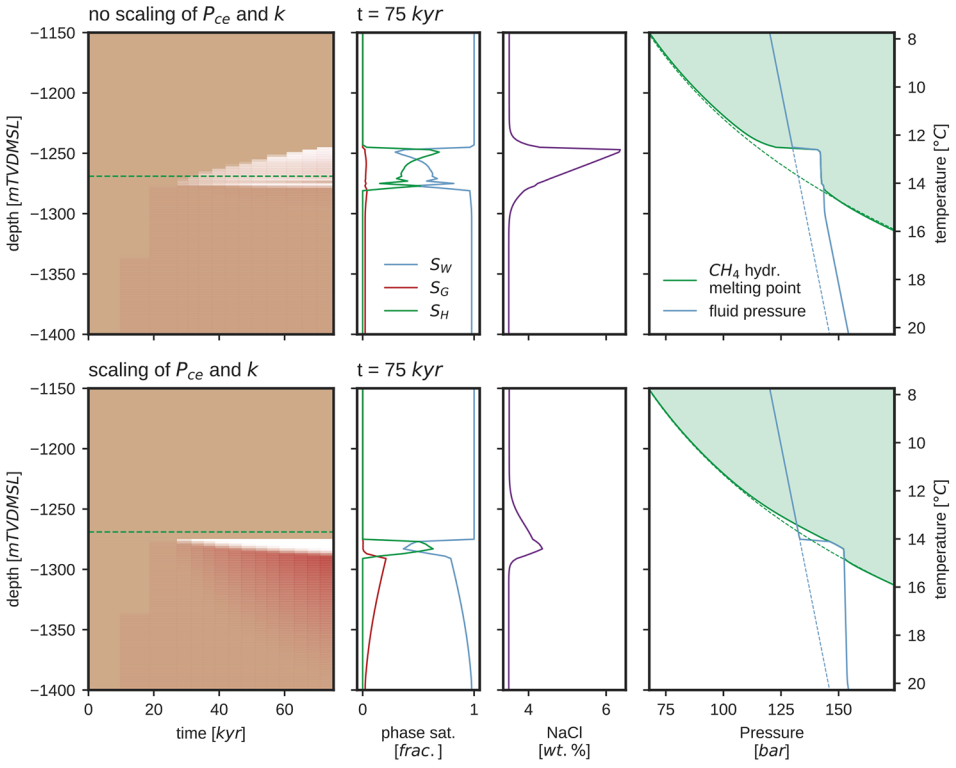

Figure 5. Cases 1A and 1B, with resulting hydrate accumulations from buoyancy-driven gas flow. The top row shows results for an accumulation where scaling of transport properties is not considered. The bottom row shows the results for an accumulation in the bottom where parameters from Table 2 were used to modify both k and P_c. From left to right, the first column shows the 1D evolution through time of hydrate (white) and gas (red) saturation. The green stippled horizontal line shows the base of the GHSZ at initial P and T conditions. The second and third columns show the distribution of phases and salinity concentrations at the end of hydrate formation (75 kyr). The last column shows the *in situ* (blue) P and T and the corresponding melting point (green) at both the beginning (stippled lines) and end (continuous lines) of the simulation. The green-shaded region highlights the P and T ranges, where hydrates are stable.

https://doi.org/10.1021/acs.energyfuels.1c03611
Energy Fuels 2022, 36, 3778−3787

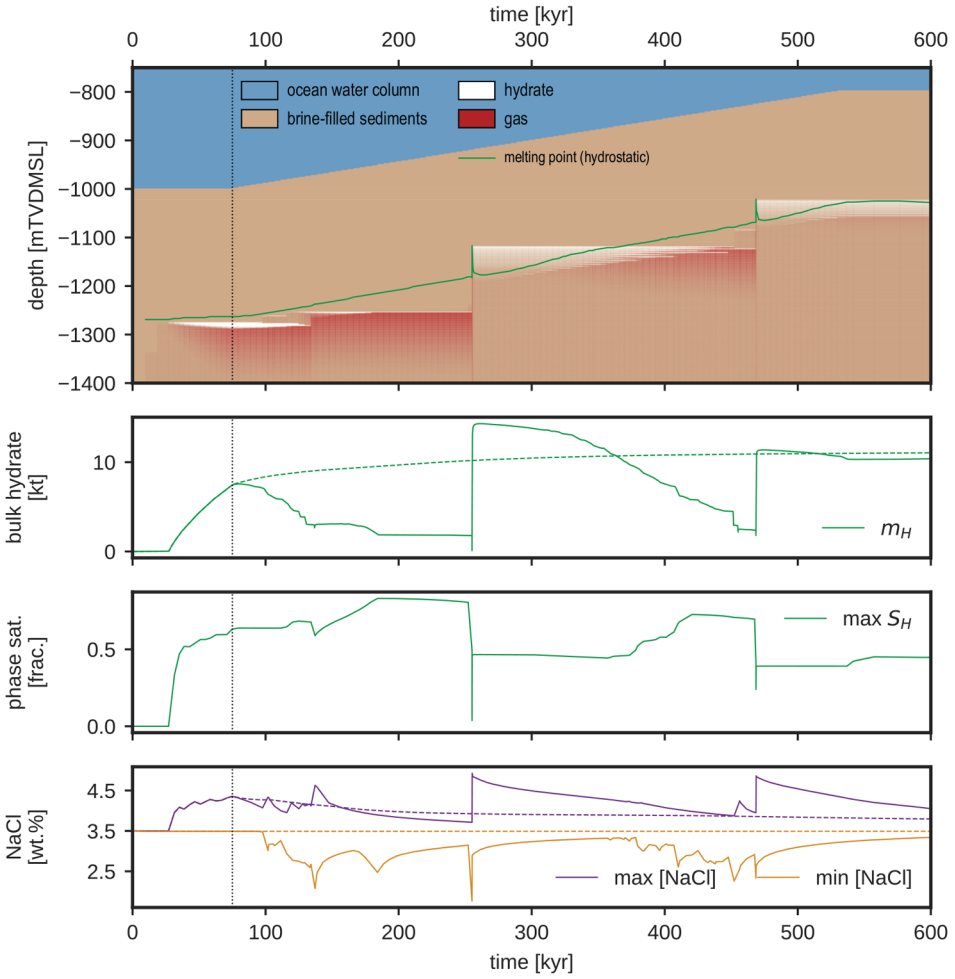

Figure 6. Case 3A, with evolution of hydrate occurrence during sedimentation (220 m/kyr). From top to bottom, the first chart shows the 1D evolution through time of hydrate (white) and gas (red) saturation. The green line shows the depth at which the temperature and pressure match the melting point at the given conditions. The second chart shows the bulk mass of hydrate through time during sedimentation (continuous) and with no sedimentation (stippled, case 2). The third chart shows the maximum hydrate saturation reached at each point in time. The fourth and last chart shows the maximum (purple) and minimum (orange) salinity during sedimentation (continuous) and with no sedimentation (stippled).

more concentrated. This is shown by how the maximum saturation of hydrates was reached toward the end of each cycle, because the bulk amount of hydrate (m_H) was at its minimum (Figure 6). After the gas column reached its maximum height, gas flowed through the hydrate layer and melted the remaining hydrate. It migrated upward, reached the shoaled base of the GHSZ, and formed new hydrates.

Figure 7 shows a detailed overview of one of these cycles. It tracks the interaction between the externally imposed temperature changes and the internal phase changes of hydrates and the resulting gas flow. The initial amount of hydrate was the result of an influx of gas migrating into the colder and shallower intervals (between points 1 and 2 in Figure 7). A peak in salinity was recorded at this instant. The melting of hydrates underneath dilutes the salinity locally, supporting the growth of more hydrates at this depth (between points 2 and 3 in Figure 7). The remaining hydrates were concentrated in a thin layer with high saturation. The peak in saturation allowed the layer to become an effective capillary seal able to support the underlying thick column of free gas. At this stage, melting was prolonged by the interplay between the variations of salinity and pressure (between points 3 and 4 in Figure 7). A very subtle increase in salinity suggests that hydrates were reformed as the capillary pressure kept increasing. Once the capillary entry pressure of the hydrate-bearing layer is overcome, the gas breaks through the seal and flows to a shallower interval, exceeding to form a new hydrate accumulation (between points 4 and 5 in Figure 7). The final melting was marked by a brief decrease in both the salinity and temperature.

When the permeability was decreased (1 μD), the simulation showed similar processes. However, the cycles were much shorter and more frequent during the same time span (Figure 8). The thickness of formed hydrate layers on each cycle was also thinner. Similarly, at a higher sedimentation rate (2 m/year), the simulation also showed a higher frequency of cycles (Figure 9) for the same thickness of sediments being deposited over time.

The process of sedimentation modeled here showed how the hydrates change as the system becomes progressively warmer. Although the hydrates are in net melting, the dynamic fluctuations of both S_H and NaCl(aq) concentration steer the rate at which fluid phases move through the system and phase changes occur, causing periods of melting and

https://doi.org/10.1021/acs.energyfuels.1c03611
Energy Fuels 2022, 36, 3778−3787

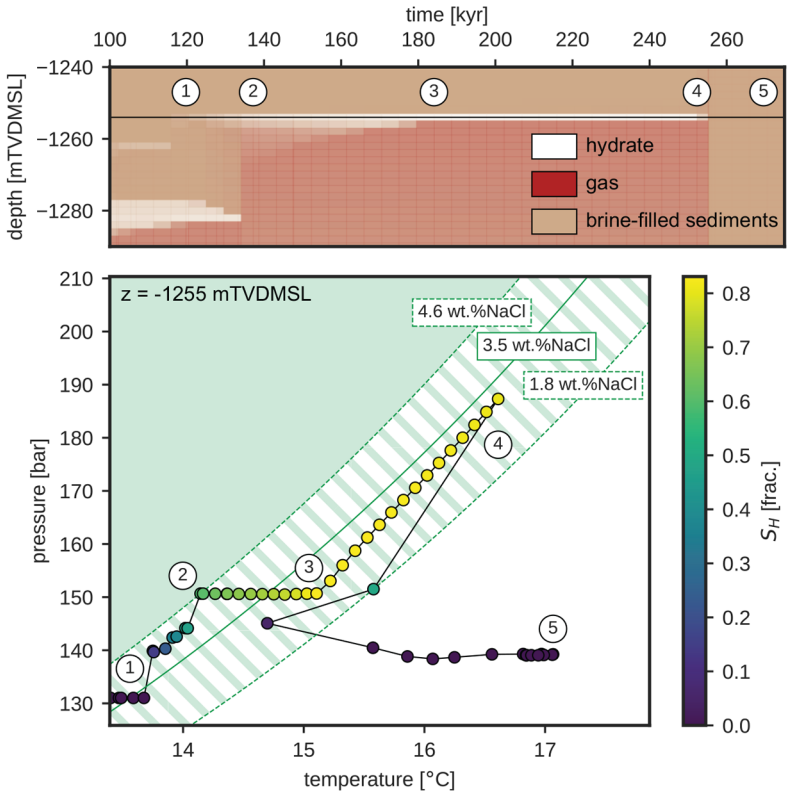

Figure 7. Case 3A, with the pressure and temperature evolution through time at 1255 mTVDMSL between 100 and 275 kyr. The top chart shows the 1D evolution through time of hydrate (white) and gas (red) saturation. The black horizontal line displays the depth at which pressure and temperature have been logged, and the circled numbers highlight the points where major changes occur in the pressure and temperature. The main chart at the bottom shows the logged pressure and temperature overlaid by the hydrate stability boundary at different salinity concentrations. The green-shaded region highlights the P and T ranges, where hydrates are stable. At point 1, hydrates start forming. Between points 2 and 3, hydrate saturation increases but salinity decreases as a result of the melting of underneath hydrates. At point 3, maximum hydrate saturation is reached, but all hydrates below this depth have melted in the system. Melting is actively occurring, but the incoming gas from underneath and the increased pressure preserve the hydrate accumulation. At point 4, the system quickly melts, salinity decreases, gas breaks through, and pressure decreases. At point 5, the system is filled by brine and residual gas.

reformation. Each cycle is initiated by gas flowing into the GHSZ and forming hydrates. The amount of methane capable of flowing is determined by the intrinsic transport properties of the sediments. In cases 3A and 4, the hydrate layers are thicker than in case 3B, where the intrinsic permeability is 100 times smaller.

The highest amount of hydrates (m_H) is reached at this point. This is reflected on the NaCl(aq) concentration reaching its peak. However, these hydrates are distributed over a thick layer, and S_H is not at its maximum. This means that the system is still permeable and can be drained by gas.

The temperature keeps increasing, and the hydrates at the deepest part of the layer are the first to melt. The higher melting point caused by the diluted brine and the availability of gas at a pressure high enough to invade the hydrate-bearing intervals result in further formation of hydrates. S_H reaches its maximum; permeability decreases; and the capillary entry pressure increases. At this point, the hydrate layer is an effective flow barrier. Both permeability and sedimentation rate can have an impact on the maximum S_H at this stage. With a lower permeability (case 3B; Figure 8), more methane remains as free gas trapped below hydrates. The larger gas column results in a higher capillary pressure, and the low permeability results in a slower rate at which more methane can turn into hydrate. The peak in S_H is also lower when the sedimentation rate is increased (case 4; Figure 9). When melting occurs at a faster rate, not enough time is given to develop a concentrated layer of hydrate with high S_H. The lower peak in S_H makes the capillary entry pressure of the hydrate-bearing layer lower and the length of the cycle shorter.

During the final stages of melting, the system goes through a period where each loss of hydrate can be compensated by gas invading the layer and forming new hydrates. No major increases are observed in S_H, but the slight increase in salinity decreases the melting point, making the hydrate progressively less stable. Because hydrates cannot support the underlying gas accumulation, the hydrate flow barrier fails and gas breaks through. When gas breakthrough occurs, the heat transported by the gas melts the remaining hydrate, reducing m_H to zero, just before a new hydrate layer is formed.

If the intrinsic permeability of the host sediments is not low (1 mD, cases 3A and 3B), gas may leak through the hydrate layer. As soon as it approaches the boundary of stability, it starts forming a new hydrate layer and, therefore, a new flow barrier. This mechanism was observed in both cases 3A and 3B, during periods where the thickness of the free gas zone was at its maximum.

Assuming that the effects of hydrate growth on sediment transport properties resemble those used in these models, the rate at which shoaling occurs is influenced by both intrinsic permeability and capillary entry pressure. Unlike the modeled sedimentation rate, shoaling occurs in pulses. The length of

https://doi.org/10.1021/acs.energyfuels.1c03611
Energy Fuels 2022, 36, 3778−3787

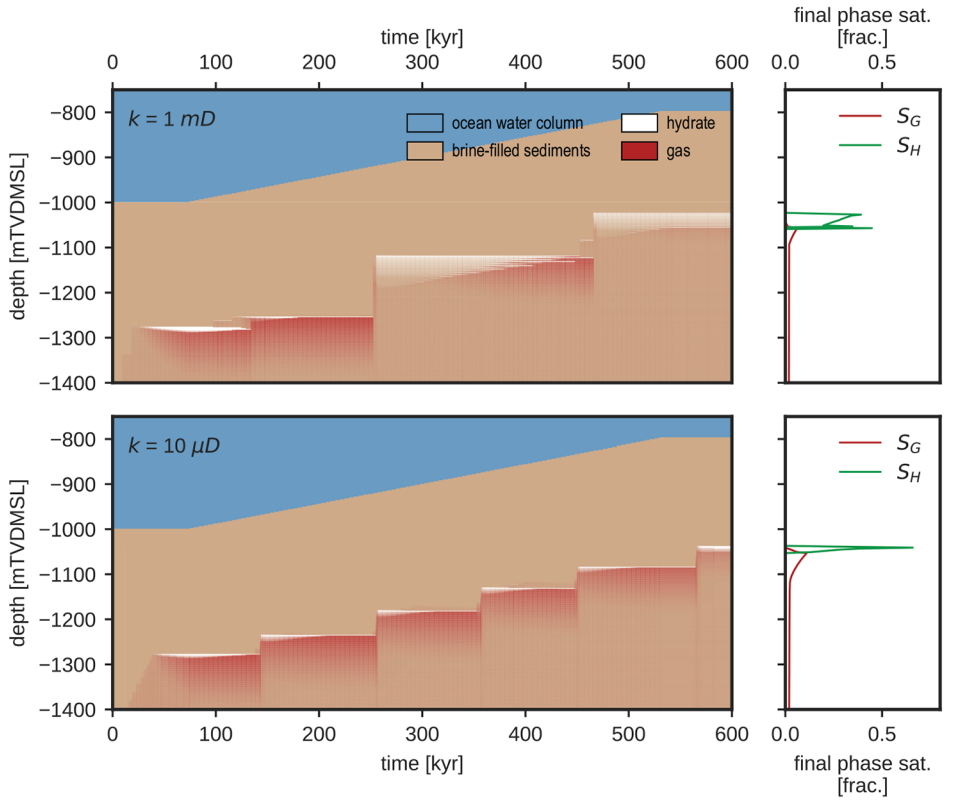

Figure 8. Comparison between cases 3A and 3B, with permeability sensitivity. On the left, hydrate evolution in the system with a permeability of 1 mD (top) and a system with a permeability of 10 μD (bottom). On the right column, final saturation of both gas (S_G) and hydrate (S_H).

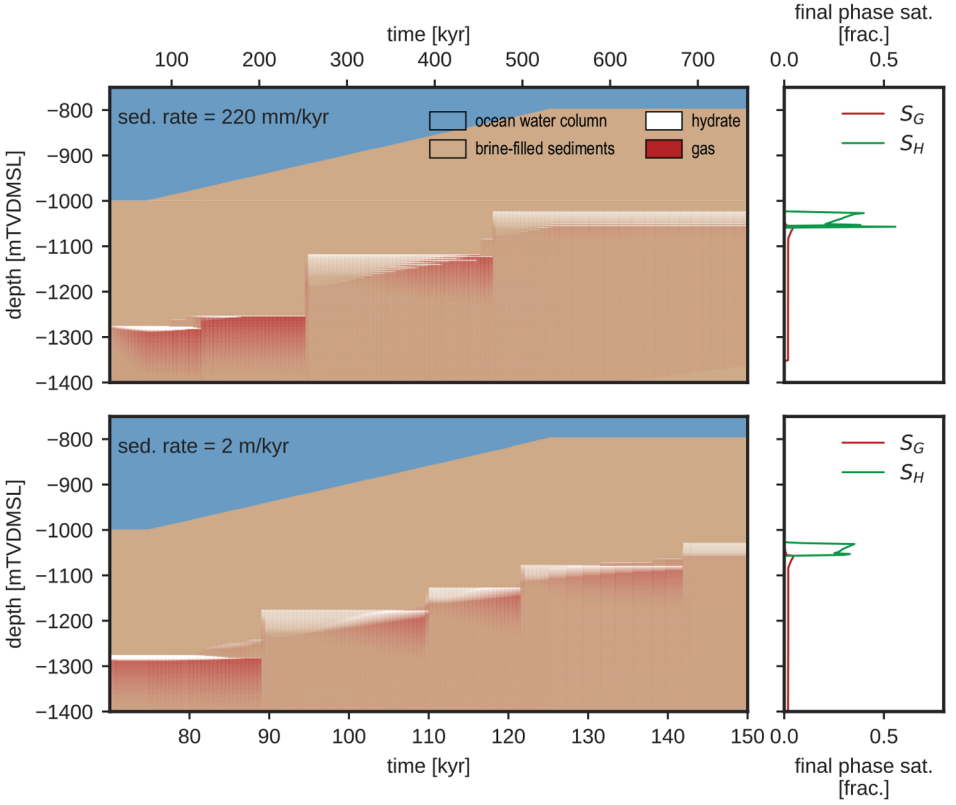

Figure 9. Comparison between cases 3A and 3C, with sedimentation rate sensitivity. On the left, hydrate evolution in a system with a sedimentation rate of 220 mm/year (top) and a sedimentation rate of 2 m/year (bottom). On the right column, final saturation of both gas (S_G) and hydrate (S_H).

https://doi.org/10.1021/acs.energyfuels.1c03611
Energy Fuels 2022, 36, 3778−3787

each pulse is a function of the heating through burial (sedimentation rate), maximum S_H, and thickness of the free gas zone.

BSR responses are normally assumed to coincide with the boundary of stability and used to derive the geothermal gradient.[39] These methods normally assume linear gradients of both pressure and temperature. However, during sedimentation, within each pulse or cycle of melting, the local pore pressure underneath the hydrate layer is actively changing. This makes the pressure gradient no longer linear or hydrostatic, particularly toward the end of each cycle. In a basin that has been experiencing sedimentation over the previous thousands of years, the characteristics of the BSR response can be affected by where, within the melting cycle, the hydrate occurrence is taking place. The identification of multiple BSR responses can be associated with those transitional periods observed in cases 3A and 4, where gas has leaked through the hydrate layer and the hydrate occurrence is shoaling.

CONCLUSION

(1) During sedimentation, a hydrate occurrence experiences pulses of melting and reformation. The length and frequency of each pulse are influenced by the rate of sedimentation and the transport properties of the host sediments. (2) Although the mechanical properties of sediments are not considered in this study, it is possible to emulate the processes of sedimentation and burial within the context of natural gas hydrate occurrences. The results are a building block in understanding the effects of hydrate formation on the transport properties of porous systems during sedimentation. (3) By keeping track of the variations in the pressure, temperature, phase saturations, and concentration of soluble components, it is possible to understand the evolution of each cycle. (4) The characteristics of a BSR response in a system that has been under active sedimentation will vary depending upon the stage of melting that the system is currently experiencing. (5) In a system with a high intrinsic capillary entry pressure, toward the end of the cycle, hydrate-bearing sediments can become a capillary seal. This results in a boundary of stability placed deeper than what the hydrostatic gradient predicts. (6) Leakage of methane through permeable hydrate layers and reformation of hydrates at shallower depths over long periods can result in double BSRs.

AUTHOR INFORMATION

Corresponding Author

Alejandro Bello-Palacios − *Department of Physics and Technology, University of Bergen, 5020 Bergen, Norway; Equinor ASA, 5020 Bergen, Norway;* orcid.org/0000-0002-0294-9485; Phone: +47-941-56-014; Email: gpb@equinor.com

Authors

Per Fotland − *Equinor ASA, 5020 Bergen, Norway*

Geir Ersland − *Department of Physics and Technology, University of Bergen, 5020 Bergen, Norway*

Complete contact information is available at: https://pubs.acs.org/10.1021/acs.energyfuels.1c03611

Notes

The authors declare no competing financial interest.

ACKNOWLEDGMENTS

This work was supported by funding from the Norwegian Research Council. Equinor ASA is thanked for permission to publish this work.

NOMENCLATURE

Abbreviations

BR = Blake Ridge
BSR = bottom simulating reflector
GHSZ = gas hydrate stability zone
GOM = Gulf of Mexico
IODP = International Ocean Discovery Program
ODP = Ocean Drilling Program
T+H = TOUGH+HYDRATE

Symbols

λ = thermal conductivity
ϕ = effective porosity (hydrate-scaled)
ϕ_0 = intrinsic porosity
ϕ_c = critical hydrate-filled porosity at which permeability is reduced to zero
ρ = density
W, G, and H = subscripts representing aqueous, gas, and hydrate phases, respectively
c_p = specific heat
k = effective permeability (hydrate-scaled)
k_0 = intrinsic permeability
k_r = relative permeability
k_{rF} = permeability reduction factor
P_c = capillary pressure
P_c^* = hydrate-scaled capillary pressure
P_{ce} = capillary entry pressure
S = phase saturation
S_{irr} = irreducible phase saturation
X_{inh} = brine salinity
aq and g = aqueous and gaseous states of aggregation
CH_4 = methane
H_2O = water
NaCl = sodium chloride
kyr = thousands of years
m = total mass
mD and μD = permeability in millidarcy and microdarcy, respectively
mTVDMSL = meters below mean sea level
P = pressure
T = temperature

REFERENCES

(1) Sloan, E. D.; Koh, C. A. *Clathrate Hydrates of Natural Gases*, 3rd ed.; CRC Press: Boca Raton, FL, 2008; Vol. *119*, Chapter 1, pp 1−28.

(2) Boswell, R.; Collett, T. S. Current perspectives on gas hydrate resources. *Energy Environ. Sci.* **2011**, *4*, 1206−1215.

(3) Collett, T. S.; Johnson, A. H.; Knapp, C. C.; Boswell, R. *Natural Gas Hydrates−Energy Resource Potential and Associated Geologic Hazards*; American Association of Petroleum Geologists (AAPG): Tulsa, OK, 2009.

(4) Boswell, R.; Collett, T. The gas hydrates resource pyramid. *Fire in the Ice* **2006**, *06*, 5−7.

(5) Paull, C. K.; Matsumoto, R.; Wallace, P. J.; Dillon, W. P. *Proceedings of the Ocean Drilling Program, Scientific Results, 164*; College Station, TX, 2000; DOI: 10.2973/odp.proc.ir.164.1996.

(6) Tréhu, A. M.; Bohrmann, G.; Torres, M. E.; Colwell, F. S. Leg 204 Synthesis: Gas Hydrate Distribution and Dynamics in the Central Cascadia Accretionary Complex. *Proceedings of the Ocean Drilling*

Program, Scientific Results, 204; College Station, TX, 2006; DOI: 10.2973/odp.proc.sr.204.101.2006.
(7) Riedel, M.; Collett, T. S.; Malone, M. Expedition 311 synthesis: Scientific findings. *Proceedings of the IODP, 311*; Washington, D.C., 2010; DOI: 10.2204/iodp.proc.311.213.2010.
(8) Karstens, J.; Haflidason, H.; Becker, L. W. M.; Berndt, C.; Rüpke, L.; Planke, S.; Liebetrau, V.; Schmidt, M.; Mienert, J. Glacigenic sedimentation pulses triggered post-glacial gas hydrate dissociation. *Nat. Commun.* **2018**, *9*, 635.
(9) Collett, T.; Bahk, J.-J.; Baker, R.; Boswell, R.; Divins, D.; Frye, M.; Goldberg, D.; Husebø, J.; Koh, C.; Malone, M.; Morell, M.; Myers, G.; Shipp, C.; Torres, M. Methane Hydrates in Nature—Current Knowledge and Challenges. *J. Chem. Eng. Data* **2015**, *60*, 319−329.
(10) You, K.; Flemings, P. B.; Malinverno, A.; Collett, T. S.; Darnell, K. Mechanisms of Methane Hydrate Formation in Geological Systems. *Rev. Geophys.* **2019**, *57*, 1146−1196.
(11) Collet, T. S.; Ladd, J. Detection of gas hydrate with downhole logs and assessment of gas hydrate concentrations (saturations) and gas volumes on the Blake Ridge with electrical resistivity log data. *Proceedings of the Ocean Drilling Program, Scientific Results, 164*; College Station, TX, 2000; DOI: 10.2973/odp.proc.sr.164.219.2000.
(12) Wu, N.; Zhang, H.; Yang, S.; Zhang, G.; Liang, J.; Lu, J.; Su, X.; Schultheiss, P.; Holland, M.; Zhu, Y. Gas Hydrate System of Shenhu Area, Northern South China Sea: Geochemical Results. *J. Geol. Res.* **2011**, *2011*, 1−10.
(13) Paull, C. K.; Matsumoto, R. Leg 164 overview. *Proceedings of the Ocean Drilling Program, Scientific Results, 164*; College Station, TX, 2000; DOI: 10.2973/odp.proc.sr.164.204.2000.
(14) Paull, C. K.; Ussle, W.; Borowski, W. S. Sources of Biogenic Methane to Form Marine Gas Hydrates In Situ Production or Upward Migration? *Ann. N. Y. Acad. Sci.* **1994**, *715*, 392−409.
(15) Liu, X.; Flemings, P. B. Dynamic multiphase flow model of hydrate formation in marine sediments. *J. Geophys. Res.* **2007**, *112*, B03101.
(16) Paull, C. K.; Ussler, W. I.; Borowski, W. S. *Sources of Biogenic Methane to Form Marine Gas Hydrates: In Situ Production or Upward Migration?*; University of North Carolina at Chapel Hill: Chapel Hill, NC, 1993; Report DOE/ER/61010--T12.
(17) Hyndman, R. D.; Spence, G. D. A seismic study of methane hydrate marine bottom simulating reflectors. *J. Geophys. Res.: Solid Earth* **1992**, *97*, 6683−6698.
(18) Wilder, J. W.; Moridis, G. J.; Wilson, S. J.; Kurihara, M.; White, M. D.; Masuda, Y.; Anderson, B. J.; Collett, T. S.; Hunter, R. B.; Narita, H. An international effort to compare gas hydrate reservoir simulators. *Proceedings of 6th International Conference on Gas Hydrates (ICGH 2008)*; Vancouver, British Columbia, Canada, July 6−10, 2008.
(19) White, M. D.; Kneafsey, T. J.; Seol, Y.; Waite, W. F.; Uchida, S.; Lin, J. S.; Myshakin, E. M.; Gai, X.; Gupta, S.; Reagan, M. T.; Queiruga, A. F.; Kimoto, S.; Baker, R. C.; Boswell, R.; Ciferno, J.; Collett, T.; Choi, J.; Dai, S.; De La Fuente, M.; Fu, P.; Fujii, T.; Intihar, C. G.; Jang, J.; Ju, X.; Kang, J.; Kim, J. H.; Kim, J. T.; Kim, S. J.; Koh, C.; Konno, Y.; Kumagai, K.; Lee, J. Y.; Lee, W. S.; Lei, L.; Liu, F.; Luo, H.; Moridis, G. J.; Morris, J.; Nole, M.; Otsuki, S.; Sanchez, M.; Shang, S.; Shin, C.; Shin, H. S.; Soga, K.; Sun, X.; Suzuki, S.; Tenma, N.; Xu, T.; Yamamoto, K.; Yoneda, J.; Yonkofski, C. M.; Yoon, H. C.; You, K.; Yuan, Y.; Zerpa, L.; Zyrianova, M. An international code comparison study on coupled thermal, hydrologic and geomechanical processes of natural gas hydrate-bearing sediments. *Mar. Pet. Geol.* **2020**, *120*, 104566.
(20) Burwicz, E.; Rüpke, L. Thermal State of the Blake Ridge Gas Hydrate Stability Zone (GHSZ)−Insights on Gas Hydrate Dynamics from a New Multi-Phase Numerical Model. *Energies* **2019**, *12*, 3403.
(21) You, K.; Flemings, P. B. Methane Hydrate Formation and Evolution during Sedimentation. *J. Geophys. Res.: Solid Earth* **2021**, *126*, e2020JB021235.
(22) Nole, M.; Daigle, H.; Cook, A. E.; Malinverno, A.; Flemings, P. B. Burial-driven methane recycling in marine gas hydrate systems. *Earth Planet. Sci. Lett.* **2018**, *499*, 197−204.
(23) Moridis, G.; Pruess, K. *User's Manual of the TOUGH+ v1. 5 Core Code: A General Purpose Simulator of Non-Isothermal Flow and Transport through Porous and Fractured Media*; Lawrence Berkeley National Laboratory (LBNL): Berkeley, CA, 2014; Report LBNL-6871E.
(24) Moridis, G. *User's Manual for the HYDRATE v1. 5 Option of TOUGH+ v1. 5: A Code for the Simulation of System Behavior in Hydrate-Bearing Geologic Media*; Lawrence Berkeley National Laboratory (LBNL): Berkeley, CA, 2014; Report LBNL-6869E.
(25) Gamwo, I. K.; Liu, Y. Mathematical Modeling and Numerical Simulation of Methane Production in a Hydrate Reservoir. *Ind. Eng. Chem. Res.* **2010**, *49*, 5231−5245.
(26) Moridis, G. J.; Collett, T. S.; Dallimore, S. R.; Satoh, T.; Hancock, S.; Weatherill, B. Numerical studies of gas production from several CH_4 hydrate zones at the Mallik site, Mackenzie Delta, Canada. *J. Pet. Sci. Eng.* **2004**, *43*, 219−238.
(27) Li, B.; Li, X.-S.; Li, G.; Chen, Z.-Y. Evaluation of gas production from Qilian Mountain permafrost hydrate deposits in two-spot horizontal well system. *Cold Reg. Sci. Technol.* **2015**, *109*, 87−98.
(28) Sun, J.; Ning, F.; Zhang, L.; Liu, T.; Peng, L.; Liu, Z.; Li, C.; Jiang, G. Numerical simulation on gas production from hydrate reservoir at the 1st offshore test site in the eastern Nankai Trough. *J. Nat. Gas Sci. Eng.* **2016**, *30*, 64−76.
(29) Jin, G.; Lei, H.; Xu, T.; Xin, X.; Yuan, Y.; Xia, Y.; Juo, J. Simulated geomechanical responses to marine methane hydrate recovery using horizontal wells in the Shenhu area, South China Sea. *Mar. Pet. Geol.* **2018**, *92*, 424−436.
(30) Zhu, H.; Xu, T.; Zhu, Z.; Yuan, Y.; Tian, H. Numerical modeling of methane hydrate accumulation with mixed sources in marine sediments: Case study of Shenhu Area, South China Sea. *Mar. Geol.* **2020**, *423*, 106142.
(31) Marín-Moreno, H.; Minshull, T. A.; Westbrook, G. K.; Sinha, B. Estimates of future warming-induced methane emissions from hydrate offshore west Svalbard for a range of climate models. *Geochem., Geophys., Geosyst.* **2015**, *16*, 1307−1323.
(32) Kowalsky, M. B.; Moridis, G. J. Comparison of kinetic and equilibrium reaction models in simulating gas hydrate behavior in porous media. *Energy Convers. Manage.* **2007**, *48*, 1850−1863.
(33) Stone, H. Probability model for estimating three-phase relative permeability. *J. Pet. Technol.* **1970**, *22*, 214−218.
(34) van Genuchten, M. T. A Closed-form Equation for Predicting the Hydraulic Conductivity of Unsaturated Soils. *Soil Sci. Soc. Am. J.* **1980**, *44*, 892−898.
(35) Henry, P.; Thomas, M.; Clennell, M. B. Formation of natural gas hydrates in marine sediments: 2. Thermodynamic calculations of stability conditions in porous sediments. *J. Geophys. Res.: Solid Earth* **1999**, *104*, 23005−23022.
(36) Day-Stirrat, R. J.; Flemings, P. B.; You, Y.; Aplin, A. C.; van der Pluijm, B. A. The fabric of consolidation in Gulf of Mexico mudstones. *Mar. Geol.* **2012**, *295*−*298*, 77−85.
(37) Davie, M. K.; Buffett, B. A. A numerical model for the formation of gas hydrate below the seafloor. *J. Geophys. Res.: Solid Earth* **2001**, *106*, 497−514.
(38) Jang, J.; Santamarina, J. C. Hydrate bearing clayey sediments: Formation and gas production concepts. *Mar. Pet. Geol.* **2016**, *77*, 235−246.
(39) Zwart, G.; Moore, J. C.; Cochrane, G. R. Variations in temperature gradients identify active faults in the Oregon accretionary prism. *Earth Planet. Sci. Lett.* **1996**, *139*, 485−495.

https://doi.org/10.1021/acs.energyfuels.1c03611
Energy Fuels 2022, 36, 3778−3787